

Supplemental Online Material to:

P-type doping of elemental bismuth with indium, gallium and tin: a novel doping mechanism in solids

Hyungyu Jin¹, Bartłomiej Wiendlocha^{1,2}, and Joseph P. Heremans^{1,3,4}

1. Department of Mechanical and Aerospace Engineering, The Ohio State University, Columbus, OH, USA
2. Faculty of Physics and Applied Computer Science, AGH University of Science and Technology, Al. Mickiewicza 30, 30-059 Krakow, Poland
3. Department of Physics, The Ohio State University, Columbus, OH, USA
4. Department of Materials Science and Engineering, The Ohio State University, Columbus, OH, USA

Table of Contents

1. Theory
 - 1.1. Details of the calculations
 - 1.2. Elemental bismuth: theory
 - 1.3. Indium-doped bismuth: theory
 - 1.4. Discussion of the doping efficiency of In in Bi
 - 1.5. Gallium-doped bismuth: theory
 - 1.6. Tin-doped bismuth: KKR-CPA results
2. Experiments
 - 2.1. Indium-doped bismuth: experiments
 - 2.1.1. Equations for galvanomagnetic phenomena, single crystals, electrons and holes
 - 2.1.2. Equations for the thermopower, with two carrier types and two scattering mechanisms
 - 2.2. Gallium-doped bismuth: experiments

1. Theory

1.1. Details of the calculations

Experimental low temperature Bi crystal structure and lattice parameters for the A7 rhombohedral primitive cell¹ were used in the computations: space group no. 166, $R\bar{3}m$, $a = 4.533\text{\AA}$, $c = 11.797\text{\AA}$ (in hexagonal notation), Bi atoms positions: (0.234, 0.234, 0.234) and (0.766, 0.766, 0.766). For the supercell full potential linearized augmented plane wave (FP-LAPW) calculations for In, Ga, and Sn doped Bi, the supercell was constructed starting from the hexagonal equivalent of the Bi unit cell (containing 6 Bi atoms). This cell was multiplied, building a $4 \times 4 \times 1$ supercell (containing 96 atoms, dimensions: $a = 18.13\text{\AA}$, $c = 11.80\text{\AA}$), whose size is equivalent to 48 primitive A7 cells. Substitution of a single Bi atom with an impurity atom results in the impurity concentration of $1.04\% \approx 1\%$, and causes lowering of the unit cell symmetry to $P3m1$ (space group no. 156), reducing the number of symmetry operations from 12 to 6. The Perdew-Burke-Ernzerhof Generalized Gradient Approximation² (PBE-GGA) was used to calculate exchange-correlation potential. In the first step, atomic positions were relaxed in a semi-relativistic computation on a $3 \times 3 \times 4$ \mathbf{k} -point mesh, and it was observed that all of the impurities (In, Ga, Sn) create a negative chemical pressure, as described in the paper. Final calculations, which included a spin-orbit coupling term, were done on a $3 \times 3 \times 5$ \mathbf{k} -point mesh.

To independently verify the results of the supercell calculations, and to study the effect of the impurity concentration on the evolution of density of states (DOS) near the Fermi energy (E_F), the Korringa-Kohn-Rostoker method, with the coherent potential approximation (KKR-CPA) was used. The advantage of the KKR-CPA is that any impurity concentration may be calculated using the same computational geometry, i.e. a primitive rhombohedral Bi crystal cell, however neglecting the local crystal relaxation effects. The KKR-CPA computations were limited to the spherical potential and semi-relativistic approximations. The DOS calculated with KKR-CPA shows good agreement with that obtained from the full potential relativistic supercell calculations. In all KKR calculations, the local density approximation (LDA) was used. The position of E_F in doped samples was obtained using the generalized Lloyd formula,³ and to increase the unit cell filling, two empty spheres were added between Bi atoms in positions along the trigonal axis: 1a (0,0,0) and 1b (0.5,0.5,0.5). Also using the KKR-CPA, we explored the behavior of possible defects in the Bi:In system, especially the role of interstitial defects.

For all calculations, high convergence limits were used on the self-consistent cycle (10^{-4} q for charge, 10^{-4} Ry for E_F and 10^{-6} Ry for the total energy). All results were checked for convergence against angular momentum cutoff and \mathbf{k} -point number.

1.2. Elemental bismuth: theory

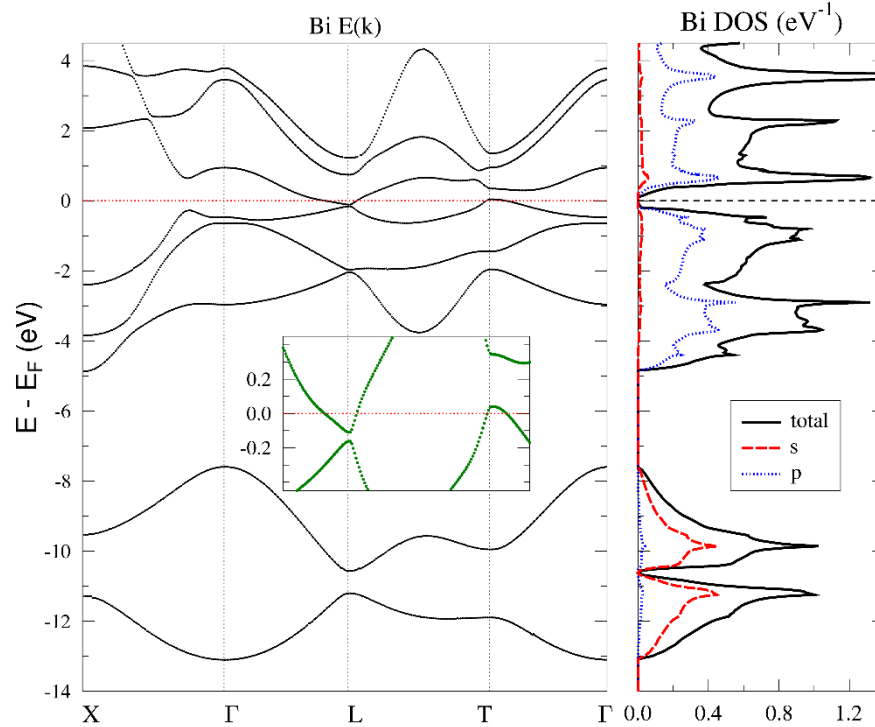


Figure S1. Electronic band structure of rhombohedral Bi from relativistic FP-KKR calculations. Inset shows the electron and hole bands near the Fermi energy E_F .

For undoped Bi, both FP-LAPW with spin-orbit coupling and fully relativistic (i.e., based on the Dirac equation) full potential KKR⁴ (FP-KKR) methods were used, giving very similar results. Electronic dispersion curves and DOS of Bi calculated by the relativistic FP-KKR are presented in Fig. S1. The two low energy-lying bands are occupied mainly by $6s$ electrons (two per each band, since there are two Bi atoms per primitive A7 cell), and the main valence block, consisting of three $6p$ -like bands, accommodates three $6p$ electrons per Bi atom. The conduction bands are separated from the valence block by the pseudo-gap. Our results are in overall good agreement with experimental finding⁵ and the previously published work.^{6,7} Relativistic effects in the band structure are visible as, for example, the splitting of the two highest valence bands at the Γ -point, while DOS near E_F is not affected much by the spin-orbit coupling. Our calculations

were not able to avoid the common LDA band-gap problem, which here manifests itself as an error in the value of the band overlap. Our calculated value of the L-T overlap is about 170 meV as the bottom of the electron band at the L-point is too low and the top of the hole band at the T-point is too high in energy. A similar value (163 meV) was obtained in the previous linear muffin-tin orbital (LMTO) calculations⁷, while the pseudopotential calculations⁶ reproduced the experimental 40 meV overlap value; the authors of that work noted this was unexpected. Considering that the common DFT+LDA error for band gaps can be of the order of 0.5 eV (e.g. in Si⁸), and that the absolute error in the band overlap here is smaller (0.13 eV), we find these values satisfactory enough to qualitatively discuss the behavior of impurities in doped systems. More rigorous quantitative analysis would require going beyond the local density methods.

1.3. Indium-doped bismuth: theory

Figure S2 shows the DOS of the nearest (NN) and next-nearest (NNN) neighbor Bi atoms to an In impurity atom. The appearance of the sharp DOS peaks around -5 eV proves that Bi electrons also contribute to the formation of the hyperdeep defect state (HDS). Since the HDS accommodates one electron from In and 1/6 of electron per each of the 3 NN and 3 NNN Bi atoms (thus one Bi electron in total) as described in the main paper (II.1), we can state that both In and Bi equally contribute to the HDS. Figure S3 shows an In impurity atom, 3 NN and 3 NNN Bi atoms, and the plane on which the charge density is projected in Fig. 3 of the main paper.

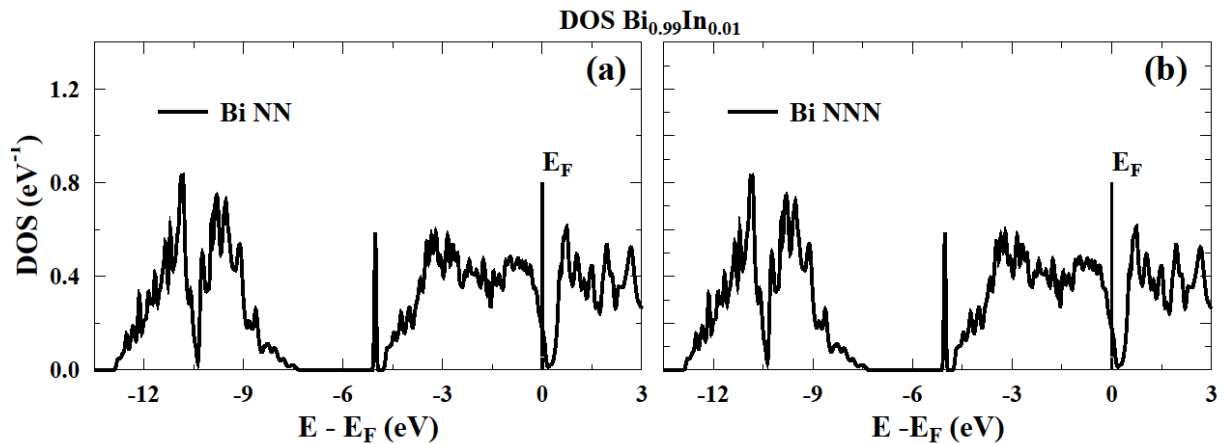


Figure S2. DOS of the (a) nearest and (b) next-nearest neighbor Bi atoms to an In impurity.

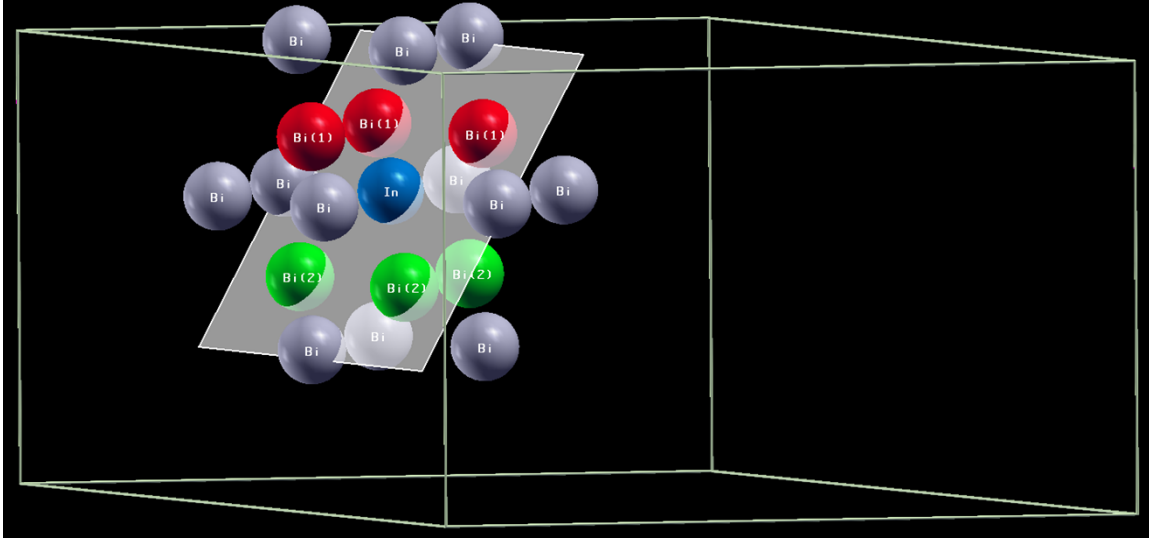


Figure S3. Neighborhood of an In atom and the plane on which the charge density is projected in Fig. 3 of the main paper. Created using XCrySDen [9].

1.4. Discussion of the doping efficiency of In in Bi

We found in III.1.1 of the main text that the doping efficiency of In is lower than that of substitutional In, which should release two holes in Bi. This indicates that not all In atoms substitute for Bi atoms, likely due to the presence of interstitial impurities in the Bi lattice that compensate the p-type doping action of substitutional In. Such behavior was previously identified for the case of Li-doped Bi,¹⁰ which showed transport properties of a degenerately doped n-type semiconductor. A simple electron count would have identified substitutional Li as an acceptor in Bi. KKR-CPA calculations¹⁰ showed that the strong n-type behavior of the Li-doped Bi samples can be explained if Li is an interstitial impurity, where it acts as a simple electron donor, rigidly moving the E_F deep into the conduction band. Here, two types of defects, the presence of interstitial In and interstitial Bi, were considered in the KKR-CPA calculations on Bi:In. In the first case, we assume that some In atoms substitute for Bi, but the rest end up being at interstitial positions. In the second case, we assume that all In atoms are at substitutional positions, but push some of Bi atoms into interstitial sites.

The largest interstitial site, the 1a (0,0,0) site, lies between Bi atoms along the trigonal axis, and was selected for the calculations (inset in Fig. S4(a)). Fig. S4(a) shows the DOS of Bi with interstitial In atoms only. Interstitial In acts as an electron donor, moving the E_F toward the conduction band. The combination of interstitial and substitutional In in the Fig. S4(b) shows

that interstitial In compensates the acceptor behavior of the substitutional In. Here, the concentrations of the atoms in calculations were selected in order to result in the Bi:In atomic ratio as seen in the $\text{Bi}_{0.995}\text{In}_{0.005}$ substitutional case. This was done to mimic the experimental condition where only the Bi:In atomic ratio is controlled. Interstitial In gives one electron to the main valence block, and for small In concentrations $\sim 0.1\%$, E_F moves according to this number. For higher concentrations near the pseudo-gap, interstitial In acts more effectively, and the position of E_F moves approximately as if it had the valence up to three for $\sim 1\%$.

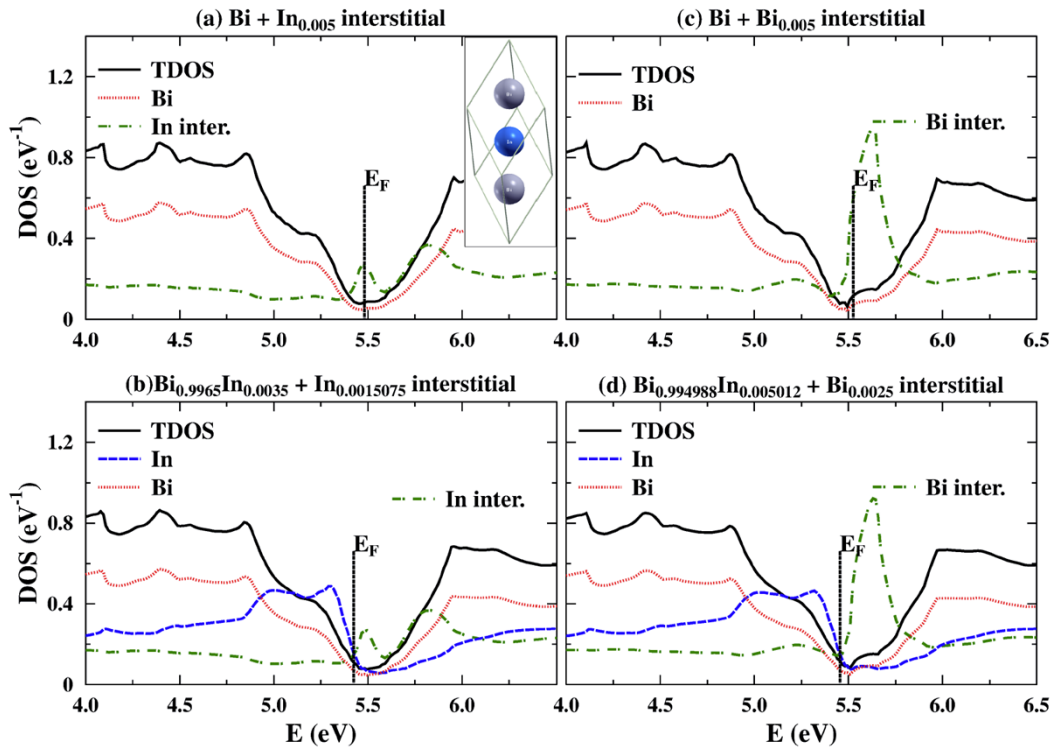


Figure S4. KKR-CPA density of states (DOS) for Bi and $\text{Bi}_{1-\alpha}\text{In}_\alpha$ with defects: (a) interstitial In in undoped Bi, (b) interstitial In in $\text{Bi}_{1-\alpha}\text{In}_\alpha$, (c) interstitial Bi in undoped Bi, (d) and interstitial Bi in $\text{Bi}_{1-\alpha}\text{In}_\alpha$. The inset in (a) shows an In atom (blue ball) located at the interstitial site between Bi atoms (gray balls) in the rhombohedral unit cell of Bi. The random-looking concentrations are from the attempt to keep the atomic ratio close to the $\text{Bi}_{0.995}\text{In}_{0.005}$ case.

A similar behavior is observed in the second case, that of interstitial Bi (Fig. S4(c) and (d)). Generally, interstitial Bi is a strong electron donor, with the valence number up to three, and in combination with the substitutional In, this pair behaves as an n-type impurity. Thus, to

make the system p-type, the number of interstitial Bi should be at least two times smaller than the number of substitutional In.

In either case, the behavior of the Bi:In system with defects is not a simple rigid shift of E_F , which makes it difficult to define a precise valence number of the defects. Even so, a meaningful conclusion can be drawn from this defect study: either interstitial In or interstitial Bi may lead to the carrier compensation effects and explain the low efficiency observed for In doping in Bi.

1.5. Gallium-doped bismuth: theory

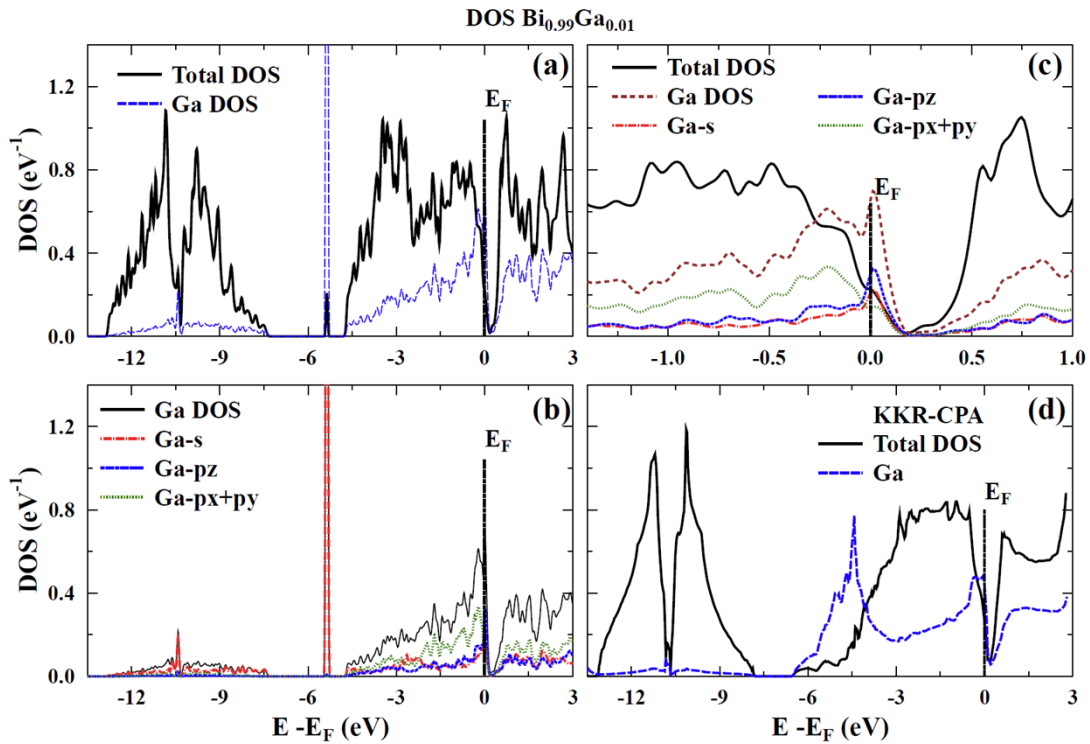


Figure S5. Density of states (DOS) for $Bi_{0.99}Ga_{0.01}$. (a-c) FP-LAPW supercell results, (d) KKR-CPA result.

A set of calculations as were performed on In-doped Bi were also applied to Ga-doped Bi, with the same technical details. Being a smaller atom than In, substitutional Ga creates a stronger relaxation effect when placed in the Bi matrix: the nearest neighbors move from 3.06 Å to 2.89 Å and the next nearest from 3.51 Å to 3.38 Å. Nevertheless, this difference does not alter the main features of the DOS of the doped system. Fig. S5(a) and (b)

show the formation of the HDS DOS peak in the supercell study, with no formation of the resonant deep defect state (DDS) near E_F (Fig. S5(c)). As in the case of Bi:In, the HDS peak is also present in the KKR-CPA results, but broadened and overlapped with the valence band DOS (Fig. S5(d)). The acceptor behavior of Ga is well seen in Fig. S6, where E_F moves deeper into the valence band upon increasing the concentration of Ga atoms. Therefore, clear similarity between In and Ga doped Bi is observed, in agreement with the experimental observations shown later. This suggests that the p-type doping mechanism via creation of an HDS is not limited to the Bi:In case, and is likely to be applied to other dopants and host materials.

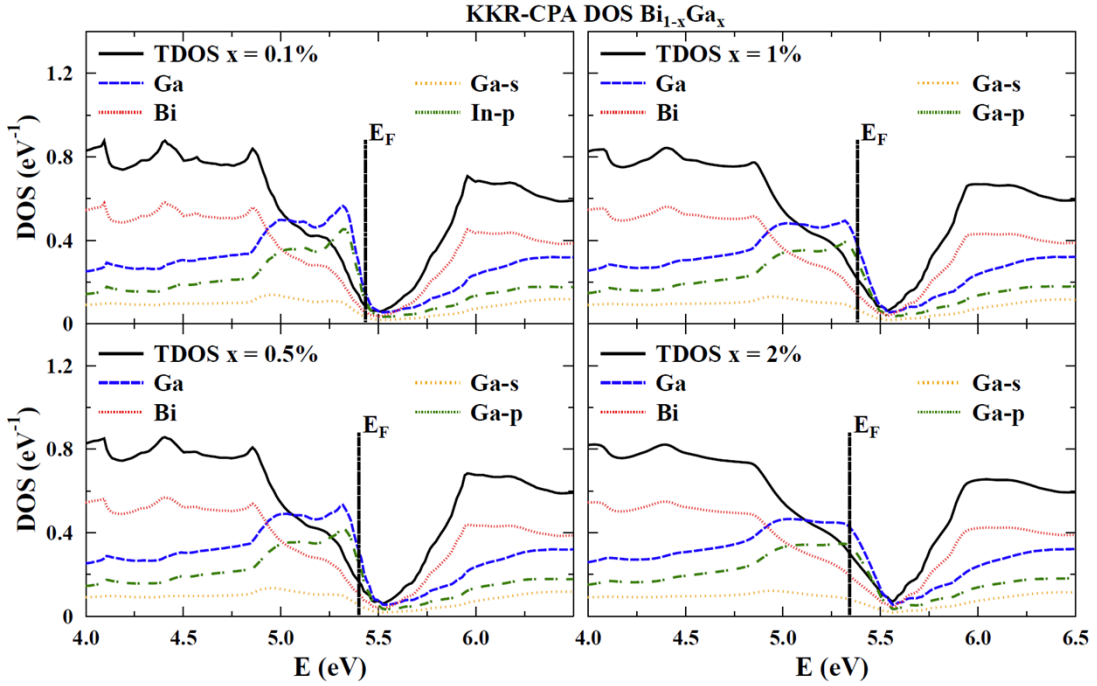


Figure S6. Evolution of density of states (DOS) for the Bi:Ga from the KKR-CPA calculations. The Ga and Bi atomic contributions are given per atom, not multiplied by the concentrations.

1.6. Tin-doped bismuth: KKR-CPA results

The KKR-CPA total and atom-decomposed DOS near E_F for 0.1%, 0.5%, 1%, and 2% substitutional Sn in Bi are presented in Fig. S7, where contributions from Sn s - and p -states are also plotted. We again observe the confirmation of acceptor behavior of Sn and the absence of DDS formation (i.e. there are no partial DOS peaks near E_F).

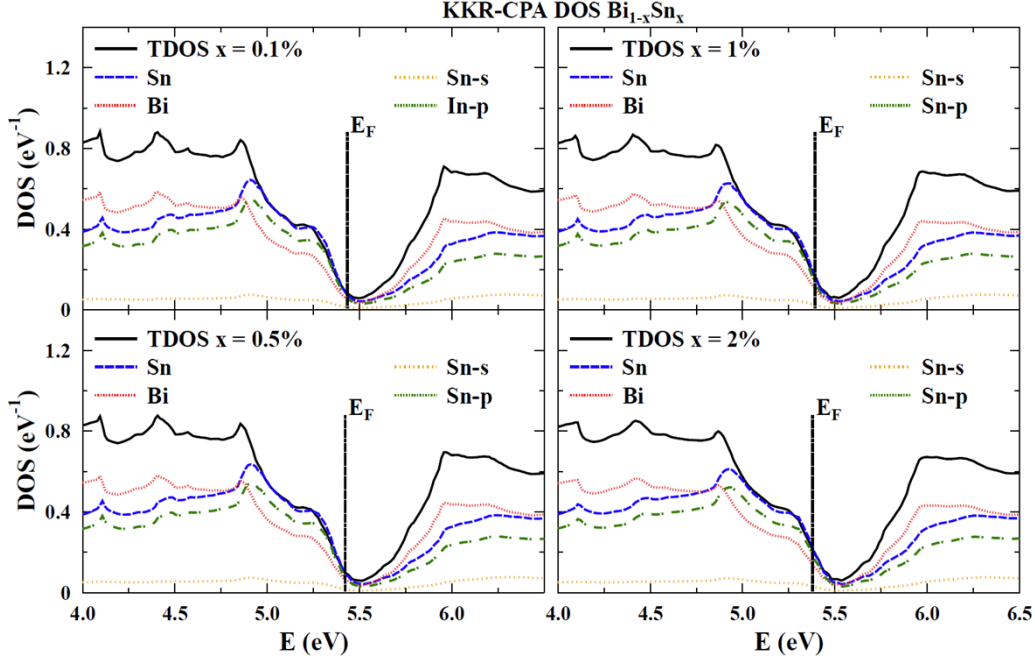


Figure S7. Evolution of density of states (DOS) for the Bi:Sn from the KKR-CPA calculations. The Sn and Bi atomic contributions are given per atom, not multiplied by the concentrations. Modifications of DOS near E_F are closer to rigid band like, compared to the In and Ga cases.

2. Experiments

2.1. Indium-doped bismuth: experiments

2.1.1. Equations for galvanomagnetic phenomena, single crystals, electrons and holes

Here we report the detailed analysis of the Hall measurement for Bi:In samples shown in Fig. 6(b) in the main text. In elemental Bi single crystals, electrons of density N dominate the low-field Hall coefficient¹¹ when the conditions $\mu_x\mu_y B_z^2 \cong 1$ and $\nu^2 B_z^2 < 1$ hold simultaneously. Here, μ_x and μ_y are the electron mobilities taken for each electron ellipsoid along the x (binary) and y (bisectrix) axes, respectively [inset in Fig. 6(a)], and ν is the isotropic hole mobility in the xy -plane. In this regime, we observe a negative slope in $\rho_{xy}(B_z)$ for both Bi:In samples [inset in Fig. 6(b)]. In contrast, $\rho_{xy}(B_z)$ becomes nearly linear in B_z with a positive slope at higher fields where $\nu^2 B_z^2 > 1$, which indicates that holes of density P now dominate. The slope of each curve corresponds to Hall coefficient R_H of each sample. In the low-field limit, R_H yields the electron concentration, while in the high-field limit, R_H reflects the excess hole concentration. In this

case, $\lim_{B \rightarrow 0} R_H = -C / Nq$ and $\lim_{B \rightarrow \infty} R_H = C / (P - N)q$, where q is the electron charge and C is the Hall prefactor for the $\rho_{xy}(B_z)$ configuration, given by^{12,13}:

$$C = 4 \left(\mu_x \mu_y - \frac{P}{N} v^2 \right) \left(\mu_x + \mu_y + 2 \frac{P}{N} v \right)^{-2} \quad \text{* MERGEFORMAT (S1).}$$

When $B_z \rightarrow 0$, Eq. (S1) can be reduced to $C = 4\mu_x\mu_y / (\mu_x + \mu_y)^2$. By inserting mobility values for pure Bi taken from Ref. [12] at 4.2 K, $C \cong 0.1$. Here, we assumed that the ratio μ_x / μ_y is not affected by In doping, which is justified, since the ratio between the electron effective masses near the Fermi energy is not affected either. Additionally, it is observed that variation in C from 4.2 K to 10 K is negligible.¹² Therefore, the same $C \cong 0.1$ is used for $T = 2$ K in Fig. 6(b) of the main text. When $B_z \rightarrow \infty$, $\rho_{xy}(B_z)$ becomes linear and thus, R_H saturates, indicating that the material becomes degenerate. In degenerate semiconductors or semimetals with spherical constant energy surfaces $C = 1$ [Ref. 14]. N and $(P-N)$ for each In-doped sample can be calculated using the obtained R_H and C , and these are the values reported in Table II of the main paper.

2.1.2. Equations for the thermopower, with two carrier types and two scattering mechanisms

A model is developed here to compute the total thermopower of a system with both electrons and holes, each of which is subject to two scattering mechanisms. As in the main text, the index ϕ refers to the scattering by acoustical phonons, while the index r refers to the scattering due to the added impurity. When there are both electrons and holes, the total S for each crystallographic direction can be expressed as

$$S = \frac{S_e \sigma_e + S_h \sigma_h}{\sigma_e + \sigma_h} \quad \text{(S2),}$$

where $S_e (< 0)$ and $S_h (> 0)$ are the partial thermopowers of electrons and holes, respectively. Moreover, in a similar way with the Matthiessen's rule, one can combine S for different scattering mechanisms using the Gorter-Nordheim rule:

$$S = \frac{S_\phi/\mu_\phi + S_r/\mu_r}{1/\mu_\phi + 1/\mu_r} \quad (\text{S3}).$$

From Eq. (S2) and (S3), an expression for the total S of the In-doped samples is found for each direction:

$$S = \frac{Nq \left[\frac{S_{e\phi}/\mu_\phi + S_{er}/\mu_r}{(1/\mu_\phi + 1/\mu_r)^2} \right] + Pq \left[\frac{S_{h\phi}/\nu_\phi + S_{hr}/\nu_r}{(1/\nu_\phi + 1/\nu_r)^2} \right]}{Nq \left(\frac{\mu_\phi + \mu_r}{\mu_\phi \mu_r} \right)^{-1} + Pq \left(\frac{\nu_\phi + \nu_r}{\nu_\phi \nu_r} \right)^{-1}} \quad (\text{S4}).$$

To evaluate the partial thermopowers, which are isotropic,¹⁵ the variation of the E_F with temperature can be computed from the known effective masses and temperature dependence of N and P . Heremans *et al.*¹⁶ introduced a pseudo-parabolic model for Bi which takes into account the non-parabolicity of the conduction band at the L-point, as well as the temperature dependence of electron effective masses. In the model, the relation between the Fermi energy, as measured from the band edge, E_F , and N is given by

$$N = \frac{16\pi}{3h^3} (2 \det \mathbf{m}_e)^{1/2} \int_0^\infty \gamma(E)^{3/2} \left(-\frac{\partial f_0}{\partial E} \right) dE \quad (\text{S5}).$$

Here, \mathbf{m}_e is the band-edge mass tensor of electrons, whose determinant is the cube of the density of states mass, $\gamma(E) = E(1 + E/E_G)$ where E_G is the gap in the energy spectrum, and f_0 is the Fermi distribution function.

While the model has been successfully applied to explain the behavior of Sn-doped Bi samples,¹⁷ the authors found that it does not provide an adequate temperature dependence of E_F at high temperature. The difficulty lies in the unknown temperature dependence of the heavy electron mass along the bisectrix direction. We observe that the pseudo-parabolic model works even at high temperatures when the temperature dependence of the electron effective mass is ignored while the non-parabolicity is kept.¹⁶ Therefore, in our calculation, the mass determinant in Eq. (S5) was assumed to be temperature independent. The partial thermopower of electrons, a scalar, is given by the pseudo-parabolic model¹⁶ as

$$S_e = -\frac{k_B}{q} \left[\frac{\left(\frac{5}{2} + \lambda\right) F_{3/2+\lambda}(\eta_F) + \left(\frac{7}{2} + \lambda\right) F_{5/2+\lambda}(\eta_F) / \eta_G}{\left(\frac{3}{2} + \lambda\right) F_{1/2+\lambda}(\eta_F) + \left(\frac{5}{2} + \lambda\right) F_{3/2+\lambda}(\eta_F) / \eta_G} - \eta_F \right] \quad (\text{S6}),$$

where λ is the scattering parameter, defined as the exponent of the energy dependence of the relaxation time $\tau \propto E^\lambda$, F is the Fermi integral:

$$F_r = \int_0^\infty \frac{\eta^r}{1 + \exp(\eta - \eta_F)} d\eta \quad (\text{S7}),$$

and η_F and η_G denote $E_F / k_B T$ and $E_G / k_B T$, respectively. As regards the T-point holes, the dispersion can be effectively described by the parabolic model for which equations are obtained by setting $E_G \rightarrow \infty$ in Eq. (S5) and (S6):

$$P = \frac{16\pi}{3h^3} (2 \det \mathbf{m}_h)^{1/2} \int_0^\infty E^{3/2} \left(-\frac{\partial f_0}{\partial E} \right) dE \quad (\text{S8}).$$

$$S_h = \frac{k_B}{q} \left[\frac{\left(\frac{5}{2} + \lambda\right) F_{3/2+\lambda}(\eta_F)}{\left(\frac{3}{2} + \lambda\right) F_{1/2+\lambda}(\eta_F)} - \eta_F \right] \quad (\text{S9}).$$

With the known temperature dependence of N and P , the temperature dependence of E_F for electrons and holes can be found from Eq. (S5) and (S8). Those E_F 's are in turn substituted into Eq. (S6) and (S9) to yield the partial thermopowers for electrons and holes, respectively. For undoped Bi, $\lambda = -1/2$ denoting the acoustical phonon scattering, while $\lambda = 0$ is added for the In-doped sample to account for the effect from the energy-independent neutral impurity scattering. The resistivity provides evidence for temperature-independent scattering, which implies the energy-independent character of the scattering mechanism.

2.2. Gallium-doped bismuth: experiments

One polycrystalline sample of Bi, to which 0.5 at. % Ga was added, was prepared in a vacuum sealed ampoule. The ampoule was heated to 903 K and then rapidly quenched. This method usually does not result in a polycrystalline alloy with fine and randomly-oriented grains, because, upon solidification, the liquidus front progresses radially inward, which leads to a slight preferential crystallographic orientation of the grains in the final sample. This is difficult to

characterize quantitatively, so that measurements of strongly anisotropic properties are sample-dependent and thus unreliable. We confine the results here to comparing the Ga-doped sample to a similarly-prepared undoped Bi sample, and to an analysis of the zero-field resistivity and the Hall effect, which reveals the density of the majority and minority carriers no matter what the crystal orientation is.¹⁸ The possibility of Ga segregation was studied by DSC, but, contrary to the case of Bi:In, no Ga segregation was detected down to 10 ppm level. Therefore, we assume that most of 0.5 at. % Ga has been dissolved in the Bi matrix.

The zero-field $\rho(T)$ of the Bi:Ga sample resembles that of Bi:In showing a bump at 45 K, whereas the undoped polycrystalline Bi sample exhibits a metal-like behavior (Fig. S8(a)). The overall magnitude of $\rho(T)$ of Bi:Ga is larger compared to that of Bi:In, indicating enhanced alloy scattering, possibly because the difference in Pauling electronegativity is larger between Bi and Ga than between Bi and In. Fig. S8(b) shows that the Hall resistivity ρ_H is a linear function of magnetic field (B) at the high field regime where $\bar{v}^2 B^2 > 1$, which suggests that holes, of density P , dominate. We use the notation $\bar{v}, \bar{\mu}$ to denote the mobility of holes and electrons, respectively, averaged over all crystallographic directions. On the other hand, in the low field limit where the conditions $\bar{\mu}^2 B^2 \cong 1$ and $\bar{v}^2 B^2 < 1$ hold simultaneously, we observe a negative slope in $\rho_H(B)$ (inset in Fig. S8(b)), indicating the presence of a small number (N) of high mobility minority electrons.

The method used by Issi¹⁸ to characterize two-band conduction in undoped Bi polycrystals with $P=N$ is quite different from the method described in the main text (III.1.2) with Eqs. (1-2) for single crystals; we copy it here and extend it to the case where $P \neq N$. When two-band conduction is considered, the four parameters to be fitted are the electron density N and mobility $\bar{\mu}$, and the hole density P and mobility \bar{v} . The electrical conductivity ($\sigma = 1/\rho$) at zero field is the sum of the contribution of electrons and holes:

$$\sigma = \sigma_e + \sigma_h, \quad \sigma_e = Nq\bar{\mu}, \quad \sigma_h = Pq\bar{v} \quad (\text{S10}).$$

The relative transverse (i.e. with the current flow perpendicular to B) magnetoresistance is fitted with two parameters a and b to a magnetic field dependence:

$$\frac{\rho(B) - \rho(B=0)}{\rho(B=0)} = \frac{aB^2}{1 + bB^2} \quad (\text{S11}),$$

where parameters a and b are given by:

$$\begin{aligned}
a &= \frac{1}{q} \frac{\sigma_e \sigma_h}{(\sigma_e + \sigma_h)^2} (\bar{\mu} + \bar{\nu})^2 \\
b &= \frac{1}{q^2} \frac{(\sigma_e \sigma_h)^2}{(\sigma_e + \sigma_h)^2} \frac{(N - P)^2}{N^2 P^2}
\end{aligned}
\tag{S12}.$$

Here, the experimental value of parameter b is only reliable in the high field limit, whereas a can be fitted at intermediate with good accuracy. As was the case for single crystals, the expected saturation of $\rho(B)$ at high field is not always observed, which forces us to refrain from using b . Therefore, a measurement of the magnetic field dependence of the Hall resistivity $\rho_H(B)$ is added (Fig. S8(b)) for the four parameter fit. Again, following Issi¹⁸:

$$\rho_H = \frac{B}{q} \frac{q^2 (P\bar{\nu}^2 - N\bar{\mu}^2) + B^2 \frac{\sigma_e^2 \sigma_h^2}{q^2} \frac{P - N}{N^2 P^2}}{\sigma^2 + B^2 \frac{\sigma_e^2 \sigma_h^2}{q^2} \frac{(P - N)^2}{N^2 P^2}}
\tag{S13},$$

which we can separate into a low-field Hall coefficient $R_{H0} \equiv \lim_{\bar{\mu}B, \bar{\nu}B \rightarrow 0} (\rho_H / B)$ and a high-field

Hall coefficient $R_{H\infty} \equiv \lim_{\bar{\mu}B, \bar{\nu}B \rightarrow \infty} (\rho_H / B)$ given by:

$$\begin{aligned}
R_{H0} &= \frac{q (P\bar{\nu}^2 - N\bar{\mu}^2)}{\sigma^2} \\
R_{H\infty} &= \frac{1}{q} \frac{1}{P - N}
\end{aligned}
\tag{S14}.$$

The final step is to use experimental values of ρ , a , R_{H0} , and $R_{H\infty}$ to derive values of P , N , $\bar{\mu}$, and $\bar{\nu}$. For Ga-doped polycrystalline Bi, we find $N \cong 9.4 \times 10^{15} \text{ cm}^{-3}$ and $P \cong 1.3 \times 10^{18} \text{ cm}^{-3}$ at 2 K, with mobility values of $\bar{\mu} \approx (5 \pm 1) \times 10^5 \text{ cm}^2 \text{V}^{-1} \text{s}^{-1}$ from 6 K to 60 K, and $\bar{\nu} \approx 1 \times 10^5 \text{ cm}^2 \text{V}^{-1} \text{s}^{-1}$ below 10 K, which decreases to $\bar{\nu} \approx 2.5 \times 10^4 \text{ cm}^2 \text{V}^{-1} \text{s}^{-1}$ at 60 K. The carrier concentrations are shown in Fig. S8(c) as a function of temperature. Above 60 K, the full model does not result in unique and accurate values for the properties of the minority electrons, but the excess hole concentration ($P - N$) can still be obtained accurately just by using $R_{H\infty}$ in Eq. (S14). The data confirm that Ga, another group III element, also behaves as an acceptor in Bi, and its doping efficiency (i.e. the number of holes per Ga atom) is estimated to be higher than that of In. The similarity in the behavior of $\rho(T)$, and the high mobility of the electrons, which is temperature-

independent below 60 K, reveals that Ga introduces the energy-independent neutral impurity scattering in Bi that In does.

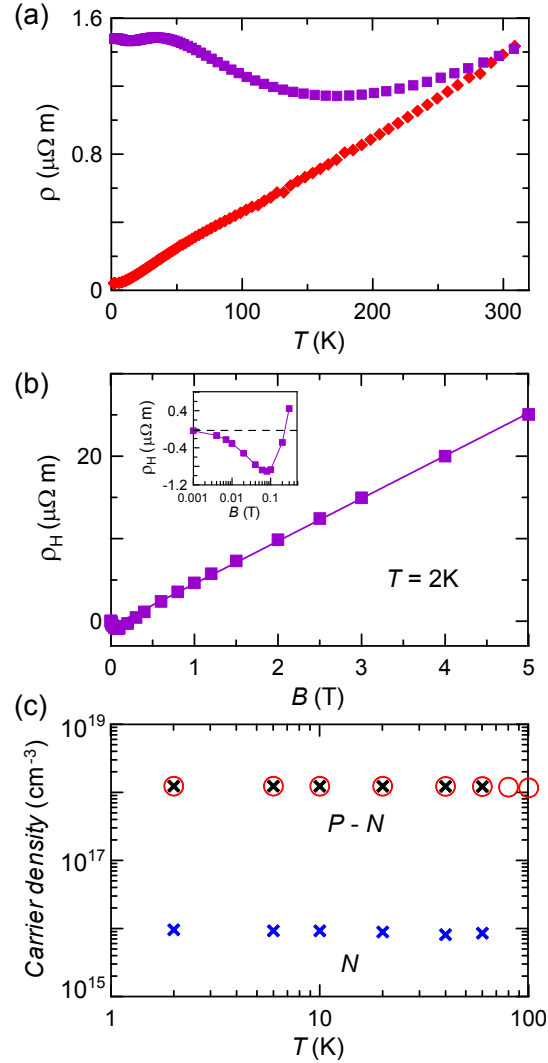


Figure S8. (a) Temperature dependence of the electrical resistivity ρ of undoped Bi and $\text{Bi}_{99.5}\text{Ga}_{0.5}$ polycrystalline samples. The symbols are the experimental data: (red diamond) undoped Bi, (purple square) $\text{Bi}_{99.5}\text{Ga}_{0.5}$. (b) Hall resistivity $\rho_H(B)$ versus magnetic field for $\text{Bi}_{99.5}\text{Ga}_{0.5}$ sample measured at 2K. The points indicate the experimental data, while the lines are added to guide the eye. The inset contains magnification of $\rho_H(B)$ at low magnetic field, which shows the transition from the negative slope to the positive slope. (c) Temperature dependence of the electron (N) and excess hole ($P - N$) densities for $\text{Bi}_{99.5}\text{Ga}_{0.5}$ sample. The cross symbols are the data obtained by solving Eqs. (S10-S14), and the circle symbols indicate the excess hole density calculated from the slope of $\rho_H(B)$ at high magnetic field (i.e. $R_H \propto$ in Eq. (S14)).

References

- ¹ P. Cucka and C. S. Barrett, *Acta Cryst.*, 1962, **15**, 865.
- ² J. P. Perdew, K. Burke, and M. Ernzerhof, *Phys. Rev. Lett.*, 1996, **77**, 3865.
- ³ S. Kaprzyk and A. Bansil, *Phys. Rev. B*, 1990, **42**, 7358.
- ⁴ K. Kutorasinski, B. Wiendlocha, J. Tobola, and S. Kaprzyk, *Phys. Rev. B*, 2014, **89**, 115205.
- ⁵ V. S. Edel'man and M. S. Khaikin, *Zh. Eksp. Teor. Fiz.*, 1965, **49**, 107 [*Sov. Phys. JETP*, 1966, **22**, 77].
- ⁶ X. Gonze, J. P. Michenaud, and J. P. Vigneron, *Phys. Rev. B*, 1990, **41**, 11827.
- ⁷ A. B. Shick, J. B. Ketterson, D. L. Novikov, and A. J. Freeman, *Phys. Rev. B*, 1999, **60**, 15484.
- ⁸ R. W. Godby, M. Schlüter, and L. J. Sham, *Phys. Rev. Lett.*, 1986, **56**, 2415.
- ⁹ A. Kokalj, *Comp. Mater. Sci.*, 2003, **28**, 155. Code available from <http://www.xcrysden.org/>.
- ¹⁰ C. M. Orovets, A. M. Chamoire, H. Jin, B. Wiendlocha, and J. P. Heremans, *J. Electron. Mater.*, 2012, **41**, 1648.
- ¹¹ J. M. Noothoven van Goor, *Philips Research Reports Suppl.*, 1971, **4**, 1-91.
- ¹² R. Hartman, *Phys. Rev.*, 1969, **181**, 1070.
- ¹³ B. Abeles and S. Meiboom, *Phys. Rev.*, 1956, **101**, 544.
- ¹⁴ Yu. I. Ravich, B. A. Efimova, and I. A. Smirnov, *Semiconducting lead chalcogenides*, Plenum Press, New York, 1970.
- ¹⁵ C. F. Gallo, B. S. Chandrasekhar, and P. H. Sutter, *J. Appl. Phys.*, 1963, **34**, 144.
- ¹⁶ J. P. Heremans and O. P. Hansen, *J. Phys. C: Solid State Phys.*, 1979, **12**, 3483.
- ¹⁷ J. P. Heremans and O. P. Hansen, *J. Phys. C: Solid State Phys.*, 1983, **16**, 4623.
- ¹⁸ J-P. Issi, PhD Thesis, Université Catholique de Louvain, Belgium, 1965.